All-Pass-Filter-Based PLL Systems

Linear Modeling, Analysis, and Comparative Evaluation

Golestan, Saeed; Guerrero, Josep M.; Vasquez, Juan C.; Abusorrah, Abdullah M.; Al-Turki, Yusuf

Published in:
IEEE Transactions on Power Electronics

DOI (link to publication from Publisher):
10.1109/TPEL.2019.2937936

Publication date:
2020

Document Version
Accepted author manuscript, peer reviewed version

This article has been accepted for publication in a future issue of this journal, but has not been fully edited. Content may change prior to final publication. Citation information: DOI 10.1109/TPEL.2019.2937936, IEEE Transactions on Power Electronics

All-Pass-Filter-Based PLL Systems: Linear Modeling, Analysis, and Comparative Evaluation

Saeed Golestan, *Senior Member, IEEE*, Josep M. Guerrero, *Fellow, IEEE*, Juan C. Vasquez, *Senior Member, IEEE*, Abdullah M. Abusorrah, *Senior Member, IEEE*, and Yusuf Al-Turki, *Senior Member, IEEE*

***Abstract*—All-pass filter (APF) passes all frequency components of a signal without altering their amplitude, but changes their phase. This feature has made the APF a versatile building block in different signal processing applications. The focus of this paper is on APF-based phase-locked loops (PLLs), where the APF is required for creating a 90° phase shift at the fundamental frequency. Such a phase shift is needed for generating a fictitious orthogonal signal in single-phase applications and rejecting the grid voltage imbalance in three-phase systems. To the best of authors' knowledge, none of the APF-based PLLs have an accurate model yet. This gap in knowledge makes the analysis of these synchronization systems and identifying their advantages/disadvantages compared to state-of-the-art structures complicated. The main objective of this paper is to bridge this knowledge gap.**

***Index Terms*—All-pass filter (APF), modeling, phase-locked loop (PLL), quadrature signal generation (QSG), single-phase systems, synchronization, three-phase systems.**

I. Introduction

POWER ELECTRONIC converters are widely used in different applications, such as renewable energy systems, uninterruptible power supplies, power quality conditioners, and electric vehicles among others [1], [2]. Depending on the application in hand, these converters may have different control systems. Almost all of them, however, require a synchronization unit in their controllers. Such a unit may be designed in different ways. A popular method is using the phase-locked loop (PLL) concept [3]–[5].

PLLs are nonlinear closed-loop control systems with a long history of use in power and energy applications. Focusing on single-phase applications, PLLs are divided into two major categories [3]: Quadration signal generation-based PLLs (QSG-PLLs), which mimic the operating principle of a three-phase synchronous reference frame PLL (SRF-PLL) by producing a 90°-phase-shifted version of the single-phase input signal, and power-based PLLs (pPLLs), which employ a product-type phase detector. In power applications, which this paper focuses on, QSG-PLLs have received more attention than pPLLs [3].

Manuscript received May 14, 2018; accepted July 15, 2019.

S. Golestan, J. M. Guerrero, and J. C. Vasquez are with the Department of Energy Technology, Aalborg University, Aalborg DK-9220, Denmark (e-mail: sgd@et.aau.dk; joz@et.aau.dk; juq@et.aau.dk).

A. M. Abusorrah and Y. Al-Turki are with the Department of Electrical and Computer Engineering, Faculty of Engineering, and Center of Research Excellence in Renewable Energy and Power Systems, King Abdulaziz University, Jeddah, Saudi Arabia (e-mail: aabusorrah@kau.edu.sa; yaturki@yahoo.com).

Color versions of one or more of the figures in this paper are available online at http://ieeexplore.ieee.org.

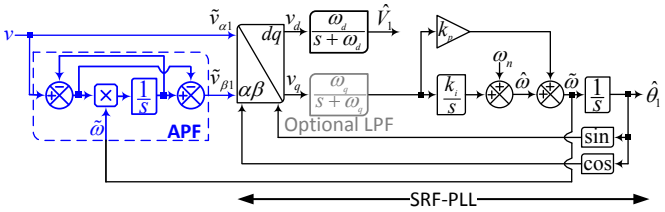

Fig. 1. Block diagram of the 1ϕ-APF-PLL. v is the single-phase input signal. k_p and k_i are the control parameters of the proportional-integral (PI) controller. ω_d and ω_q are the cutoff frequency of low-pass filters (LPFs) in the d- and q-axis, respectively. The q-axis LPF is optional. ω_n is the nominal angular frequency of the input signal. $\tilde{\omega}$ and $\hat{\omega}$ are both estimations of the input signal angular frequency, and $\hat{\theta}_1$ and $\hat{V}_1$ are estimations of its phase angle and amplitude, respectively.

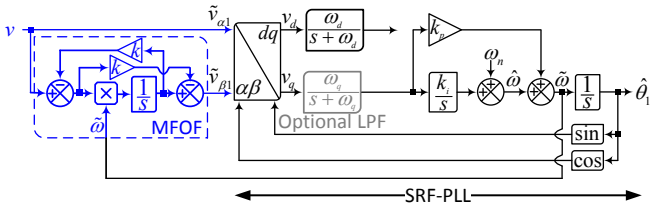

Fig. 2. Block diagram of the MFOF-PLL. The parameter k is an additional degree of freedom. See the caption of Fig. 1 for the description of other parameters.

A large number of QSG-PLLs have been presented in the literature [3]. The key difference between these PLLs lies in how to produce the quadrature signal mentioned above. Using transfer delay [6], [7], second-order generalized integrator [8]–[10], inverse Park transform [10], [11], and all-pass filter (APF) [12]–[14] are notable examples.

The APF is a filter that passes all frequency components without affecting their amplitude, but changes their phase. Using the APF for generating the quadrature signal in single-phase PLLs dates back to more than a decade ago [12]–[14]. Fig. 1 illustrates the block diagram of the single-phase APF-based PLL (1ϕ-APF-PLL), which consists of a first-order APF for generating the quadrature signal and an SRF-PLL. Notice that the SRF-PLL has an optional LPF in its q-axis. Notice also that a frequency feedback loop, which is connected to the output of the PI controller, adapts the APF to frequency changes.

In [15], adding a degree of freedom (parameter k) to the 1ϕ-APF-PLL structure has been proposed. Fig. 2 illustrates this idea, which is referred to as the modified first-order filter-

This article has been accepted for publication in a future issue of this journal, but has not been fully edited. Content may change prior to final publication. Citation information: DOI 10.1109/TPEL.2019.2937936, IEEE Transactions on Power Electronics

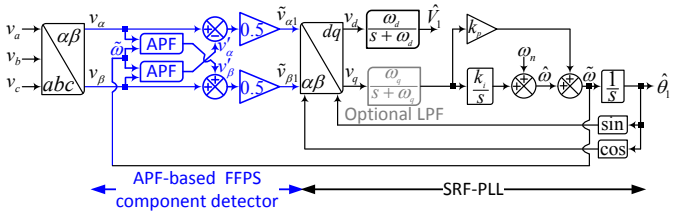

Fig. 3. Block diagram of the 3ϕ-APF-PLL.

based PLL (MFOF-PLL) [15].[1] Notice that the 1ϕ-APF-PLL is a special case of the MFOF-PLL with $k = 1$. Notice also that the MFOF frequency response converges to that of an integrator and differentiator when the parameter k tends to zero and infinity, respectively.

The APF application is not limited to single-phase PLLs. In fact, around two decades ago, its application for rejecting the grid voltage imbalance in three-phase PLLs has been proposed in [16]. Fig. 3 illustrates this idea, which is referred to as the three-phase APF-based PLL (3ϕ-APF-PLL).[2] The 3ϕ-APF-PLL includes an APF-based fundamental-frequency positive-sequence (FFPS) detector, which works based on instantaneous symmetrical components theory, and an SRF-PLL.

To the best of authors' knowledge, no accurate model for the 1ϕ-APF-PLL, MFOF-PLL, and 3ϕ-APF-PLL has yet been presented.[3] Without such a model, the analysis of these synchronization systems and identifying their shortcomings and advantages compared to state-of-the-art structures are complicated. This paper aims to bridge this gap in knowledge.

II. 3ϕ-APF-PLL

The 3ϕ-APF-PLL [Fig. 3], as mentioned before, consists of an APF-based FFPS component detector and an SRF-PLL. The FFPS component detector works based on the instantaneous symmetrical components theory in the stationary ($\alpha\beta$) frame. According to this theory, the FFPS component of an imbalanced vector in the $\alpha\beta$ frame can be extracted by applying the following transformation [18]:

$$\begin{bmatrix} \tilde{v}_{\alpha 1}(t) \\ \tilde{v}_{\beta 1}(t) \end{bmatrix} = 0.5 \begin{bmatrix} 1 & -q \\ q & 1 \end{bmatrix} \begin{bmatrix} v_{\alpha}(t) \\ v_{\beta}(t) \end{bmatrix} \tag{1}$$

where $q = e^{-j\pi/2}$. The 90° phase-shift operator q in the 3ϕ-APF-PLL is implemented using a first-order APF.

[1]In the original structure of the MFOF-PLL in [15], the signal $\hat{\omega}$ is used for feeding back to the MFOF. Here, for the sake of consistency with the 1ϕ-APF-PLL structure, the frequency feedback point is changed to the signal $\tilde{\omega}$ (see Fig. 2).

[2]In the original structure of 3ϕ-APF-PLL (see [16, Fig. 5]), the APF-based FFPS component detector is implemented in the *abc* frame, which demands three APFs. A better way, as shown in Fig. 3, is implementing that in the $\alpha\beta$ frame, which requires only two APFs.

[3]Some attempts to model the 1ϕ-APF-PLL and the MFOF-PLL have been made before (see [17, Fig. 2] and [15, Fig. 5]). These models, however, are not accurate and, therefore, may not precisely predict the dynamics of the 1ϕ-APF-PLL and the MFOF-PLL.

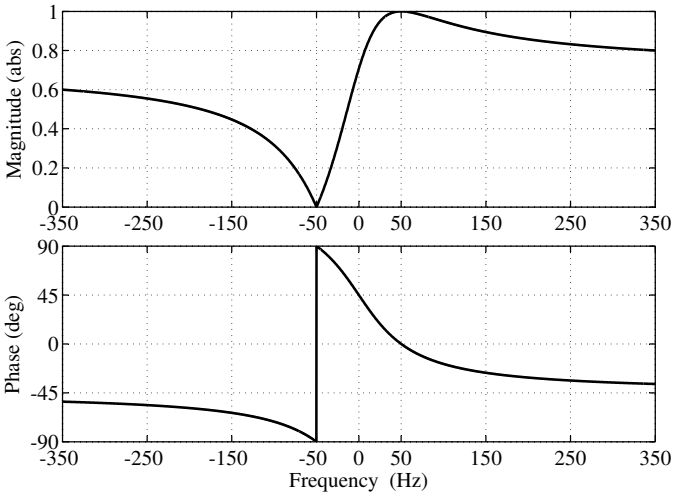

Fig. 4. Bode plot of the APF-based FFPS component detector [see (2)]. For obtaining this Bode plot, $\omega = \omega_n = 2\pi 50$ rad/s is considered.

Considering the APF transfer function as $G_{\mathrm{APF}}(s) = \frac{\omega - s}{\omega + s}$, (1) can be rewritten in the space vector notation as follows:

$$[\tilde{v}_{\alpha 1}(s) + j\tilde{v}_{\beta 1}(s)] = \frac{1}{2}\left[1 + j\frac{\omega - s}{\omega + s}\right][v_{\alpha}(s) + jv_{\beta}(s)]\,. \tag{2}$$

Fig. 4 shows the Bode plot of the transfer function (2). As expected, it has unity gain with zero phase at +50 Hz, and zero gain at -50 Hz, which confirms that it is an FFPS component detector.

A. Modeling

Assume that the three-phase input signals of the 3ϕ-APF-PLL are as follows:

$$\begin{aligned} v_a(t) &= V_1 \cos(\theta_1) \\ v_b(t) &= V_1 \cos(\theta_1 - 2\pi/3) \\ v_c(t) &= V_1 \cos(\theta_1 + 2\pi/3) \end{aligned} \tag{3}$$

where V_1 and θ_1 are the grid voltage fundamental amplitude and phase angle, respectively. Applying Clarke's transformation to (3) gives the $\alpha\beta$-axis input of the APF-based FFPS component detector as

$$\begin{aligned} v_{\alpha}(t) &= V_1 \cos(\theta_1) \\ v_{\beta}(t) &= V_1 \sin(\theta_1). \end{aligned} \tag{4}$$

Considering (4) and Fig. 4, the $\alpha\beta$-axis output of the APF-based FFPS component detector can be considered as

$$\begin{aligned} \tilde{v}_{\alpha 1}(t) &= \tilde{V}_1 \cos(\tilde{\theta}_1) \\ \tilde{v}_{\beta 1}(t) &= \tilde{V}_1 \sin(\tilde{\theta}_1) \end{aligned} \tag{5}$$

where $\tilde{V}_1$ and $\tilde{\theta}_1$ are estimations of V_1 and θ_1, respectively. Based on these assumptions, the 3ϕ-APF-PLL modeling is carried out in what follows.

1) Phase Estimation Dynamics: Using (5), the phase angle of the $\alpha\beta$-axis output signals of the APF-based FFPS component detector in Fig. 3 can be expressed as

$$\tilde{\theta}_1 = \tan^{-1}\left(\frac{\tilde{v}_{\beta 1}(t)}{\tilde{v}_{\alpha 1}(t)}\right). \tag{6}$$

This article has been accepted for publication in a future issue of this journal, but has not been fully edited. Content may change prior to final publication. Citation information: DOI 10.1109/TPEL.2019.2937936, IEEE Transactions on Power Electronics

Differentiating from (6) results in

$$\frac{d\tilde{\theta}_1}{dt} = \frac{\tilde{v}_{\alpha1}(t)\frac{d\tilde{v}_{\beta1}(t)}{dt} - \tilde{v}_{\beta1}(t)\frac{d\tilde{v}_{\alpha1}(t)}{dt}}{\underbrace{\tilde{v}_{\alpha1}^2(t) + \tilde{v}_{\beta1}^2(t)}_{\tilde{V}_1^2}} \tag{7}$$

where

$$\begin{aligned}\frac{d\tilde{v}_{\alpha1}(t)}{dt} &= \frac{1}{2}\left[\frac{dv_\alpha(t)}{dt} - \frac{dv'_\alpha(t)}{dt}\right] \\ &= \frac{1}{2}\left[\frac{dv_\alpha(t)}{dt} + \frac{dv_\beta(t)}{dt} - \tilde{\omega}\left\{v_\beta(t) + 2\tilde{v}_{\alpha1}(t) - v_\alpha(t)\right\}\right] \quad (8)\end{aligned}$$

$$\begin{aligned}\frac{d\tilde{v}_{\beta1}(t)}{dt} &= \frac{1}{2}\left[\frac{dv_\beta(t)}{dt} + \frac{dv'_\beta(t)}{dt}\right] \\ &= \frac{1}{2}\left[\frac{dv_\beta(t)}{dt} - \frac{dv_\alpha(t)}{dt} + \tilde{\omega}\left\{v_\alpha(t) - 2\tilde{v}_{\beta1}(t) + v_\beta(t)\right\}\right]. \quad (9)\end{aligned}$$

Substituting (8) and (9) into (7) results in

$$\begin{aligned}\frac{d\tilde{\theta}_1}{dt} = \frac{1}{2\tilde{V}_1^2}\Bigg[&\left(\tilde{v}_{\alpha1}(t)\frac{dv_\beta(t)}{dt} - \tilde{v}_{\beta1}(t)\frac{dv_\alpha(t)}{dt}\right) \\ &+\tilde{\omega}\left(\tilde{v}_{\alpha1}(t)v_\alpha(t) + \tilde{v}_{\beta1}(t)v_\beta(t)\right) \\ &+\tilde{\omega}\left(\tilde{v}_{\alpha1}(t)v_\beta(t) - \tilde{v}_{\beta1}(t)v_\alpha(t)\right) \\ &-\left(\tilde{v}_{\alpha1}(t)\frac{dv_\alpha(t)}{dt} + \tilde{v}_{\beta1}(t)\frac{dv_\beta(t)}{dt}\right)\Bigg]. \quad (10)\end{aligned}$$

Substituting (4) and (5) into the above equation yields

$$\begin{aligned}\frac{d\tilde{\theta}_1}{dt} = \frac{1}{2}\Bigg[&\left(\frac{d\theta_1}{dt} + \tilde{\omega} + \frac{1}{V_1}\frac{dV_1}{dt}\right)\frac{V_1}{\tilde{V}_1}\sin(\theta_1 - \tilde{\theta}_1) \\ &+\left(\frac{d\theta_1}{dt} + \tilde{\omega} - \frac{1}{V_1}\frac{dV_1}{dt}\right)\frac{V_1}{\tilde{V}_1}\cos(\theta_1 - \tilde{\theta}_1)\Bigg]. \quad (11)\end{aligned}$$

Considering the definitions (12), in which Δ means a small perturbation and n refers to a nominal value, the terms of (11) can be rewritten/approximated as (13).

$$\omega = \omega_n + \Delta\omega \tag{12a}$$
$$\tilde{\omega} = \omega_n + \Delta\tilde{\omega} \tag{12b}$$
$$V_1 = V_n + \Delta V_1 \tag{12c}$$
$$\tilde{V}_1 = V_n + \Delta\tilde{V}_1 \tag{12d}$$
$$\theta_1 = \int \omega dt = \underbrace{\int \omega_n dt}_{\theta_n} + \underbrace{\int \Delta\omega dt}_{\Delta\theta_1} \tag{12e}$$
$$\tilde{\theta}_1 = \theta_n + \Delta\tilde{\theta}_1 \tag{12f}$$

$$\frac{d\tilde{\theta}_1}{dt} = \omega_n + \frac{d\Delta\tilde{\theta}_1}{dt} \tag{13a}$$

$$\begin{aligned}\frac{1}{V_1}\frac{dV_1}{dt} &= \frac{1}{V_n + \Delta V_1}\frac{d\Delta V_1}{dt} = \frac{1}{V_n}\overbrace{\frac{1}{1 + \Delta V_1/V_n}}^{\approx 1 - \Delta V_1/V_n}\frac{d\Delta V_1}{dt} \\ &\approx \frac{1}{V_n}\frac{d\Delta V_1}{dt} - \frac{1}{\boldsymbol{V_n^2}}\boldsymbol{\Delta V_1}\frac{\boldsymbol{d\Delta V_1}}{\boldsymbol{dt}} \approx \frac{1}{V_n}\frac{d\Delta V_1}{dt} \quad (13b)\end{aligned}$$

$$\frac{d\theta_1}{dt} + \tilde{\omega} = 2\omega_n + \frac{d\Delta\theta_1}{dt} + \Delta\tilde{\omega} \tag{13c}$$

$$\begin{aligned}\frac{V_1}{\tilde{V}_1} &= \frac{V_n + \Delta V_1}{V_n + \Delta\tilde{V}_1} = \frac{1 + \Delta V_1/V_n}{1 + \Delta\tilde{V}_1/V_n} \\ &\approx (1 + \Delta V_1/V_n)(1 - \Delta\tilde{V}_1/V_n) \\ &= 1 + \Delta V_1/V_n - \Delta\tilde{V}_1/V_n - \boldsymbol{\Delta V_1\Delta\tilde{V}_1/V_n^2} \\ &\approx 1 + \Delta V_1/V_n - \Delta\tilde{V}_1/V_n \quad (13d)\end{aligned}$$

$$\sin(\theta_1 - \tilde{\theta}_1) \approx (\Delta\theta_1 - \Delta\tilde{\theta}_1) \tag{13e}$$
$$\cos(\theta_1 - \tilde{\theta}_1) \approx 1 \tag{13f}$$

Notice that the highlighted terms in (13) are negligible.

By substituting (13) into (11) and neglecting the multiplication of small perturbations, we have

$$\begin{aligned}\frac{d\Delta\tilde{\theta}_1}{dt} \approx \omega_n\left(\Delta\theta_1 - \Delta\tilde{\theta}_1\right) + \frac{\omega_n}{V_n}\left(\Delta V_1 - \Delta\tilde{V}_1\right) + \frac{1}{2}\frac{d\Delta\theta_1}{dt} \\ -\frac{1}{2V_n}\frac{d\Delta V_1}{dt} + \frac{1}{2}\Delta\tilde{\omega}. \quad (14)\end{aligned}$$

2) Amplitude Estimation Dynamics: Using (5), the amplitude of the $\alpha\beta$-axis output signals of the APF-based FFPS component detector in Fig. 3 can be expressed as

$$\tilde{V}_1 = \sqrt{\tilde{v}_{\alpha1}^2(t) + \tilde{v}_{\beta1}^2(t)}. \tag{15}$$

Differentiating from (15) results in

$$\frac{d\tilde{V}_1}{dt} = \frac{\tilde{v}_{\alpha1}(t)\frac{d\tilde{v}_{\alpha1}(t)}{dt} + \tilde{v}_{\beta1}(t)\frac{d\tilde{v}_{\beta1}(t)}{dt}}{\tilde{V}_1}. \tag{16}$$

Substituting (8) and (9) into (16) gives

$$\begin{aligned}\frac{d\tilde{V}_1}{dt} = \frac{1}{2\tilde{V}_1}\Bigg[&\left(\tilde{v}_{\alpha1}(t)\frac{dv_\alpha(t)}{dt} + \tilde{v}_{\beta1}(t)\frac{dv_\beta(t)}{dt}\right) \\ &-\tilde{\omega}\left(\tilde{v}_{\alpha1}(t)v_\beta(t) - \tilde{v}_{\beta1}(t)v_\alpha(t)\right) \\ &-2\tilde{\omega}\left(\tilde{v}_{\alpha1}^2(t) + \tilde{v}_{\beta1}^2(t)\right) \\ &+\tilde{\omega}\left(\tilde{v}_{\alpha1}(t)v_\alpha(t) + \tilde{v}_{\beta1}(t)v_\beta(t)\right) \\ &+\left(\tilde{v}_{\alpha1}(t)\frac{dv_\beta(t)}{dt} - \tilde{v}_{\beta1}(t)\frac{dv_\alpha(t)}{dt}\right)\Bigg]. \quad (17)\end{aligned}$$

Substituting (4) and (5) into (17) results in

$$\begin{aligned}\frac{d\tilde{V}_1}{dt} = \frac{1}{2}\Bigg[&\left(\frac{d\theta_1}{dt} + \tilde{\omega} + \frac{1}{V_1}\frac{dV_1}{dt}\right)V_1\cos(\theta_1 - \tilde{\theta}_1) \\ &-\left(\frac{d\theta_1}{dt} + \tilde{\omega} - \frac{1}{V_1}\frac{dV_1}{dt}\right)V_1\sin(\theta_1 - \tilde{\theta}_1) - 2\tilde{\omega}\tilde{V}_1\Bigg]. \quad (18)\end{aligned}$$

This article has been accepted for publication in a future issue of this journal, but has not been fully edited. Content may change prior to final publication. Citation information: DOI 10.1109/TPEL.2019.2937936, IEEE Transactions on Power Electronics

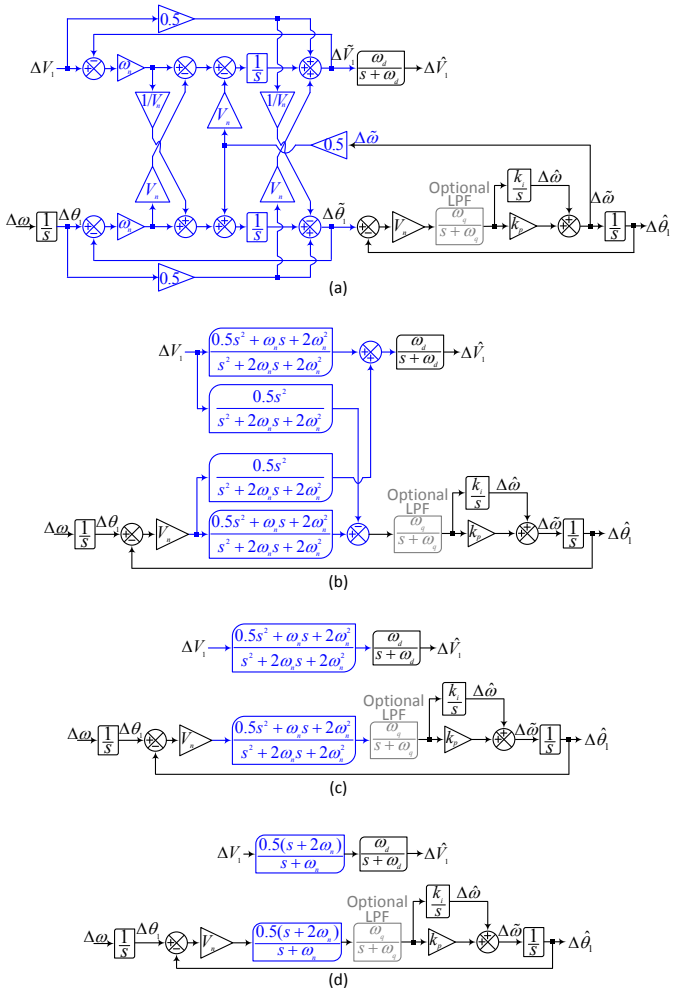

Fig. 5. (a) Full-order linear model of the 3ϕ-APF-PLL. (b) An alternative representation of the full-order model. (c) Neglecting the coupling terms of the model. (d) Reduced-order linear model of the 3ϕ-APF-PLL. All these models are linear time-invariant (LTI). It will be proved later that these models are also valid for the 1ϕ-APF-PLL.

Considering (12) and (13), (18) can be approximated by

$$\frac{d\Delta\tilde{V}_1}{dt} \approx \omega_n\left(\Delta V_1 - \Delta\tilde{V}_1\right) - \omega_n V_n\left(\Delta\theta_1 - \Delta\tilde{\theta}_1\right) + \frac{1}{2}\frac{d\Delta V_1}{dt} + \frac{V_n}{2}\frac{d\Delta\theta_1}{dt} - \frac{V_n}{2}\Delta\tilde{\omega}. \quad (19)$$

Using (14), (19), and the linear model of the SRF-PLL [19, Fig. 3], the full-order linear model of the 3ϕ-APF-PLL can be developed as shown in Fig. 5(a).

B. Model Verification

In this section, the accuracy of the full-order linear model [Fig. 5(a)] of the 3ϕ-APF-PLL is investigated. As shown in Fig. 3, there is an optional LPF in the 3ϕ-APF-PLL q-axis. The 3ϕ-APF-PLL with and without this LPF is called the 3ϕ-APF-PLL$_1$ and 3ϕ-APF-PLL$_2$, respectively. Here, for the sake of brevity, we only present the model verification results for the 3ϕ-APF-PLL$_1$. The control parameters of the 3ϕ-APF-PLL$_1$ can be found in Table I.

Three tests are considered for the model verification.

TABLE I
CONTROL PARAMETERS

	Control parameters
3ϕ-**APF-PLL**$_1$	$k_p = 130.1$, $k_i = 7014.1$, $\omega_d = 157.1$ rad/s, $\omega_q = 628.3$ rad/s
3ϕ-**APF-PLL**$_2$	$k_p = 130.1$, $k_i = 7014.1$, $\omega_d = 157.1$ rad/s
CCF-PLL	$k_p = 130.1$, $k_i = 7014.1$, $\omega_d = 157.1$ rad/s, $\omega_p = 314.2$ rad/s
1ϕ-**APF-PLL**$_1$	$k_p = 130.1$, $k_i = 7014.1$, $\omega_d = 157.1$ rad/s, $\omega_q = 628.3$ rad/s
1ϕ-**APF-PLL**$_2$	$k_p = 130.1$, $k_i = 7014.1$, $\omega_d = 157.1$ rad/s
EPLL	$\mu_p = 260.2$, $\mu_i = 14028.2$, $\mu_v = 260.2$
MFOF-PLL$_1$	$k_p = 130.1$, $k_i = 7014.1$, $\omega_d = 157.1$ rad/s, $k = 1/\sqrt{2}$
MFOF-PLL$_2$	$k_p = 130.1$, $k_i = 7014.1$, $\omega_d = 157.1$ rad/s, $k = 1$
MFOF-PLL$_3$	$k_p = 130.1$, $k_i = 7014.1$, $\omega_d = 157.1$ rad/s, $k = \sqrt{2}$

- **Test 1**: 2 Hz frequency jump.
- **Test 2**: 20° phase jump.
- **Test 3**: 0.25 p.u. voltage sag.

The results of this verification, which is conducted in Matlab/Simulink environment, are shown in Fig. 6. The solid lines are the results of the 3ϕ-APF-PLL$_1$, and the dashed lines are those predicted by its full-order linear model. The accuracy of the full-order model is remarkable. Notice that this model even predicts the coupling between amplitude and phase/frequency variables.

C. Model Order Reduction

The full-order model of the 3ϕ-APF-PLL, which is shown in Fig. 5(a), is a bit complicated for tuning its control parameters. Therefore, a reduced-order model is presented here.

Using block diagram algebra, Fig. 5(a) can be rearranged as depicted in Fig. 5(b). As the coupling between the amplitude and phase/frequency variables of the 3ϕ-APF-PLL is not that strong [see Fig. 6], it can be neglected without significantly affecting accuracy. This simplification results in Fig. 5(c). To deal with the grid voltage harmonics, the 3ϕ-APF-PLL needs to have a narrow bandwidth. It implies that the second-order transfer functions highlighted with blue color in Fig. 5(c) can be approximated in the low-frequency range by

$$\frac{0.5s^2 + \omega_n s + 2\omega_n^2}{s^2 + 2\omega_n s + 2\omega_n^2} \approx \frac{\omega_n s + 2\omega_n^2}{2\omega_n s + 2\omega_n^2} = \frac{0.5(s + 2\omega_n)}{s + \omega_n}. \quad (20)$$

This approximation leads to Fig. 5(d), which is the reduced-order model of the 3ϕ-APF-PLL.

To ensure that the reduced-order model is accurate enough, its performance in predicting the 3ϕ-APF-PLL$_1$ dynamic behavior is investigated. The same tests as those defined in Section II-B are considered for this purpose. The dotted lines in Fig. 6 show the results of the reduced-order model. Regardless of its incapability in predicting the coupling between amplitude and phase/frequency variables, it is observed that the accuracy of the reduced-order model is comparable to that of the full-order model.

D. Tuning

1) 3ϕ-APF-PLL With Optional LPF (3ϕ-APF-PLL$_1$): From the phase estimation loop of the reduced-order model [the

This article has been accepted for publication in a future issue of this journal, but has not been fully edited. Content may change prior to final publication. Citation information: DOI 10.1109/TPEL.2019.2937936, IEEE Transactions on Power Electronics

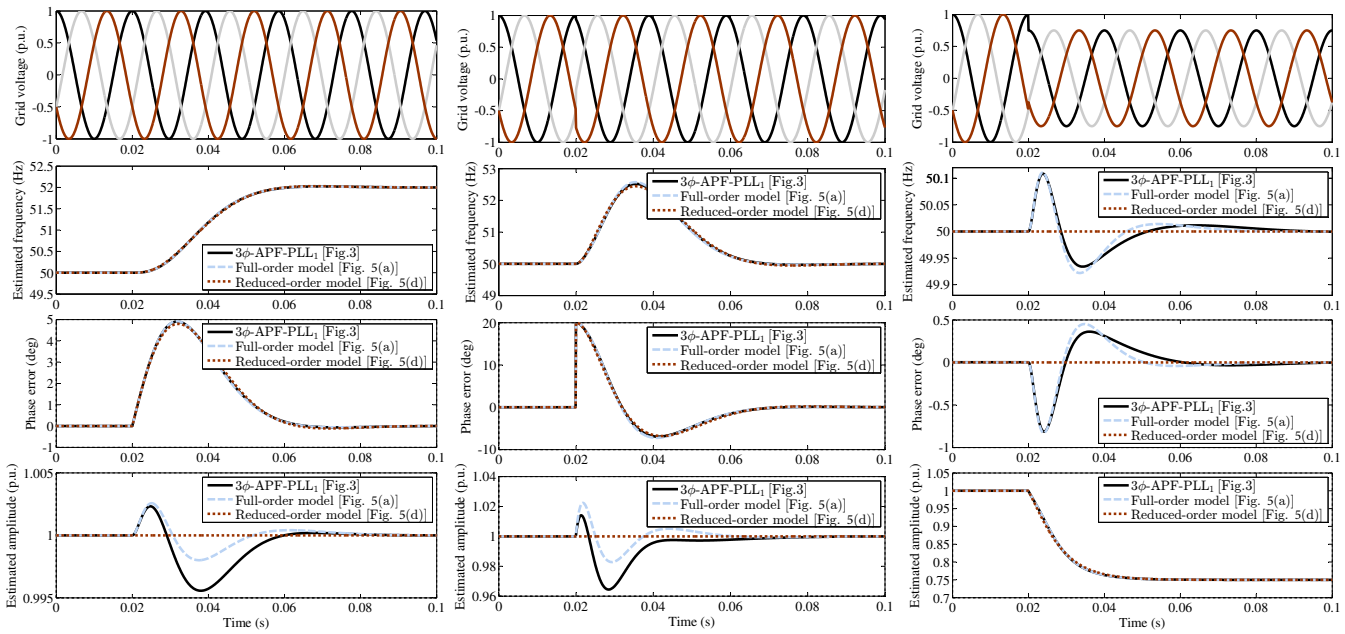

(a) (b) (c)

Fig. 6. 3ϕ-APF-PLL$_1$ model verification. (a) Test 1: 2-Hz frequency jump. (b) Test 2: 20° phase jump. (c) Test 3: 0.25-p.u. voltage sag. The estimated frequency and amplitude by the 3ϕ-APF-PLL$_1$ denote the signals $\hat{\omega}$ and $\hat{V}_1$ in Fig. 3, and the phase error is the difference of the actual and estimated phase angles. The estimated frequency, estimated amplitude, and phase error in the full-order and reduced-order models are the signals $\Delta\hat{\omega}+\omega_n$, $\Delta\hat{V}_1+V_n$, and $\Delta\theta_1-\Delta\hat{\theta}_1$, respectively. The control parameters of the 3ϕ-APF-PLL$_1$ can be found in Table I. The sampling frequency and the grid nominal frequency throughout this paper are 10 kHz and 50 Hz, respectively.

lower part of Fig. 5(d)], the following open-loop transfer function can be obtained:

$$\mathrm{G}_{ol}^{3\phi-\mathrm{APF}-\mathrm{PLL}_1}(s)=\frac{\Delta\hat{\theta}_1(s)}{\Delta\theta_1(s)-\Delta\hat{\theta}_1(s)}=V_n\frac{0.5\,(s+2\omega_n)}{s+\omega_n}\frac{\omega_q}{s+\omega_q}\frac{k_ps+k_i}{s^2}. \quad (21)$$

It is observed that selecting $\omega_q=2\omega_n=628.3$ rad/s results in a pole-zero cancellation and simplifies (21) as

$$\mathrm{G}_{ol}^{3\phi-\mathrm{APF}-\mathrm{PLL}_1}(s)=V_n\frac{\omega_n}{s+\omega_n}\frac{k_ps+k_i}{s^2}. \quad (22)$$

The open-loop transfer function (22) describes a type-2 control system (i.e., a system with two open-loop poles at the origin) with a pole-zero pair. For such a system, the symmetrical optimum method (SOM)[4] is a good option for the tuning procedure [19], [20]. Notice that the open-loop pole in (22) is already fixed. Therefore, using the SOM results in

$$k_p=\frac{\omega_c}{V_n}=\frac{\omega_n}{V_nb} \quad (23a)$$

$$k_i=\frac{\omega_c^2}{V_nb}=\frac{\omega_n^2}{V_nb^3} \quad (23b)$$

where the design constant b determines the PM value. By considering PM$=\pi/4$ rad (45°), which is recommended in [19], $b=1+\sqrt{2}$ is achieved. Substituting this value into (23), gives $k_p=130.1$ and $k_i=7014.1$.

The remaining design parameter is the cutoff-frequency ω_d, which regulates the 3ϕ-APF-PLL$_1$ amplitude estimation dynamics. A high value for this parameter makes the dynamic response of the amplitude estimation faster, but at the cost of reducing the noise immunity. Therefore, one has to make a trade-off decision. Here, based on a trial-and-error procedure, $\omega_d=w_n/2=157.1$ rad/s is selected.

2) 3ϕ-APF-PLL Without Optional LPF (3ϕ-APF-PLL$_2$): By neglecting the optional LPF in Fig. 5(d), the open-loop transfer function of the 3ϕ-APF-PLL$_2$ can be obtained as

$$\mathrm{G}_{ol}^{3\phi-\mathrm{APF}-\mathrm{PLL}_2}(s)=\frac{\Delta\hat{\theta}_1(s)}{\Delta\theta_1(s)-\Delta\hat{\theta}_1(s)}=V_n\frac{\mathbf{0.5\,(s+2\omega_n)}}{\boldsymbol{s+\omega_n}}\frac{k_ps+k_i}{s^2}. \quad (24)$$

The highlighted fraction on the right hand side of (24) is a lag filter, which models the APF dynamics. In the low-frequencies range (i.e., in frequencies less than the fundamental frequency), this term can be neglected without significantly affecting the accuracy. Therefore, in the same range, the closed-loop transfer function of the 3ϕ-APF-PLL$_2$ can be approximated by

$$\mathrm{G}_{cl}^{3\phi-\mathrm{APF}-\mathrm{PLL}_2}(s)=\frac{\Delta\hat{\theta}_1(s)}{\Delta\theta_1(s)}\approx\frac{V_nk_ps+V_nk_i}{s^2+V_nk_ps+V_nk_i}. \quad (25)$$

Using (22), the closed-loop transfer function of 3ϕ-APF-PLL$_1$ may also be approximated in the low-frequency range

[4]The SOM sets the crossover frequency at the geometric mean of the pole-zero pair (i.e., $\omega_c=\sqrt{\omega_nk_i/k_p}$) to maximize the phase margin (PM) [19], [20]. The ratio of the pole-zero pair, i.e., $b^2=\frac{\omega_n}{k_i/k_p}$, then determines the PM value as $\mathrm{PM}=\tan^{-1}\left(\frac{b^2-1}{2b}\right)$.

This article has been accepted for publication in a future issue of this journal, but has not been fully edited. Content may change prior to final publication. Citation information: DOI 10.1109/TPEL.2019.2937936, IEEE Transactions on Power Electronics

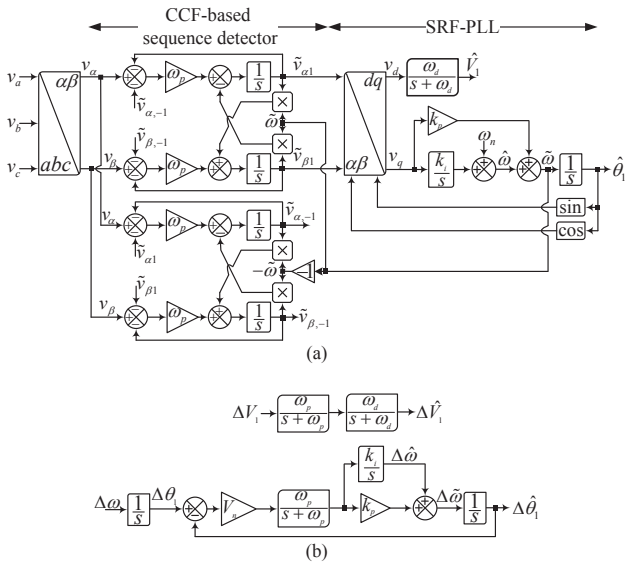

Fig. 7. (a) Block diagram of the CCF-PLL. (b) Small-signal model of the CCF-PLL.

by

$$\mathrm{G}_{cl}^{3\phi-\mathrm{APF}-\mathrm{PLL}_1}(s)=\frac{\Delta\hat{\theta}_1(s)}{\Delta\theta_1(s)}$$
$$=\frac{\omega_n(V_nk_ps+V_nk_i)}{s^3+\omega_ns^2+V_n\omega_nk_ps+V_n\omega_nk_i}$$
$$\approx\frac{\omega_n(V_nk_ps+V_nk_i)}{\omega_ns^2+V_n\omega_nk_ps+V_n\omega_nk_i}=\frac{V_nk_ps+V_nk_i}{s^2+V_nk_ps+V_nk_i}. \quad (26)$$

A comparison of (25) and (26) suggests that to have a fair comparison, k_p and k_i of the 3ϕ-APF-PLL$_2$ should be selected the same as those of the 3ϕ-APF-PLL$_1$. The same goes for the LPF cutoff frequency ω_d (see Table I).

E. Performance Assessment

In this section, a comparison among the 3ϕ-APF-PLL$_1$, 3ϕ-APF-PLL$_2$, and a complex-coefficient filter (CCF) based PLL (CCF-PLL) [21] [see Fig. 7(a)] is conducted. The CCF-PLL includes two complex band-pass filters with the center frequency at the fundamental positive-sequence and negative-sequence frequencies. These band-pass filters work collaboratively and extract the fundamental positive- and negative-sequence components of the grid voltage. The extracted FFPS component is fed to the SRF-PLL, which extracts the phase, frequency, and amplitude of this component. The estimated frequency is fed back to the complex filters to adapt them to grid frequency changes.

The small-signal model of the CCF-PLL can be observed in Fig. 7(b) [19], [22].[5] From the this model, the open-loop transfer function (27) can be obtained.

$$\mathrm{G}_{ol}^{\mathrm{CCF}-\mathrm{PLL}}(s)=\frac{\Delta\hat{\theta}_1(s)}{\Delta\theta_1(s)-\Delta\hat{\theta}_1(s)}=V_n\frac{\omega_p}{s+\omega_p}\frac{k_ps+k_i}{s^2}. \quad (27)$$

[5]It is the most accurate available model for the CCF-PLL. In obtaining this model, the dynamics of the CCF tuned at the fundamental frequency of the negative sequence has been neglected.

TABLE II
STABILITY MARGINS OF 3ϕ-APF-PLL$_1$, 3ϕ-APF-PLL$_2$, AND CCF-PLL AND DETAILS OF THEIR NUMERICAL COMPARISON

	3ϕ-**APF-PLL$_1$**	3ϕ-**APF-PLL$_2$**	**CCF-PLL**
Test A: DC offset			
Peak-to-peak frequency error	0.41 Hz	0.41 Hz	0.67 Hz
Peak-to-peak phase error	2.76°	2.75°	4.51°
Peak-to-peak amplitude error	0.04 p.u.	0.04 p.u.	0.07 p.u.
Test B: Imbalance and harmonics			
Peak-to-peak frequency error	0.02 Hz	0.08 Hz	0.02 Hz
Peak-to-peak phase error	0.15°	0.56°	0.13°
Peak-to-peak amplitude error	0.01 p.u.	0.01 p.u.	0 p.u.
Test C: Phase jump			
2% settling time	47.3 ms	54.6 ms	48.5 ms
Phase overshoot	34.73%	24.01%	39.52%
Peak frequency variation	2.52 Hz	2.24 Hz	2.68 Hz
Peak amplitude variation	0.04 p.u.	0.03 p.u.	0.06 p.u.
Test D: Frequency jump			
2% settling time	37.4 ms	40.5 ms	37.5 ms
Frequency overshoot	1.09%	1.74%	0.62%
Peak phase variation	4.9°	4.24°	5.09°
Peak amplitude variation	0 p.u.	0 p.u.	0.01 p.u.
Phase margin	43.5°	55.7°	45°

Note: All results are rounded to 2 decimal places.

Based on (22) and (27), it is immediate to conclude that to have a fair performance comparison, the proportional and integral gains of the CCF-PLL should be the same as those of the 3ϕ-APF-PLL$_1$, and the CBF gain ω_p should be equal to ω_n. Table I summarizes the control parameters of the 3ϕ-APF-PLL$_1$, 3ϕ-APF-PLL$_2$, and CCF-PLL.

Four tests are considered.

- In **Test A**, a 0.1 p.u. dc component is added to the phase A of the grid voltage.
- In **Test B**, the grid voltage is imbalanced and distorted with characteristic harmonics of order -5, $+7$, -11, and $+13$. The magnitude of all harmonics is 5%.
- In **Test C**, a 20° phase jump in the grid voltage happens.
- In **Test D**, the grid voltage experiences a 2-Hz frequency jump.

Fig. 8 shows the results of these tests, and Table II summarizes their details. According to these results, the following observations can be made:

- The 3ϕ-APF-PLL$_1$ and 3ϕ-APF-PLL$_2$ offer a higher dc-offset filtering capability than the CCF-PLL.
- The CCF-PLL and 3ϕ-APF-PLL$_2$ offer the best and worst harmonic filtering capabilities, respectively. The harmonic rejection ability of the 3ϕ-APF-PLL$_1$ is close to that of the CCF-PLL. Notice that all these PLLs completely reject the grid voltage imbalance.
- In estimating the phase and frequency variables, the 3ϕ-APF-PLL$_2$ offers a more damped dynamic response compared to the CCF-PLL and 3ϕ-APF-PLL$_1$, which is attributable to its higher phase margin [see Fig. 9].
- The estimated amplitude of the CCF-PLL experiences larger transients when phase and frequency jumps happen. It means that the coupling between the amplitude and phase/frequency variables in the CCF-PLL is stronger than that in the 3ϕ-APF-PLL$_1$ and 3ϕ-APF-PLL$_2$.

To confirm the above simulation results, Test A is repeated experimentally using the dSPACE 1006 platform. To this end, the mains voltage [which is a 50 Hz/230-V (phase RMS)

This article has been accepted for publication in a future issue of this journal, but has not been fully edited. Content may change prior to final publication. Citation information: DOI 10.1109/TPEL.2019.2937936, IEEE Transactions on Power Electronics

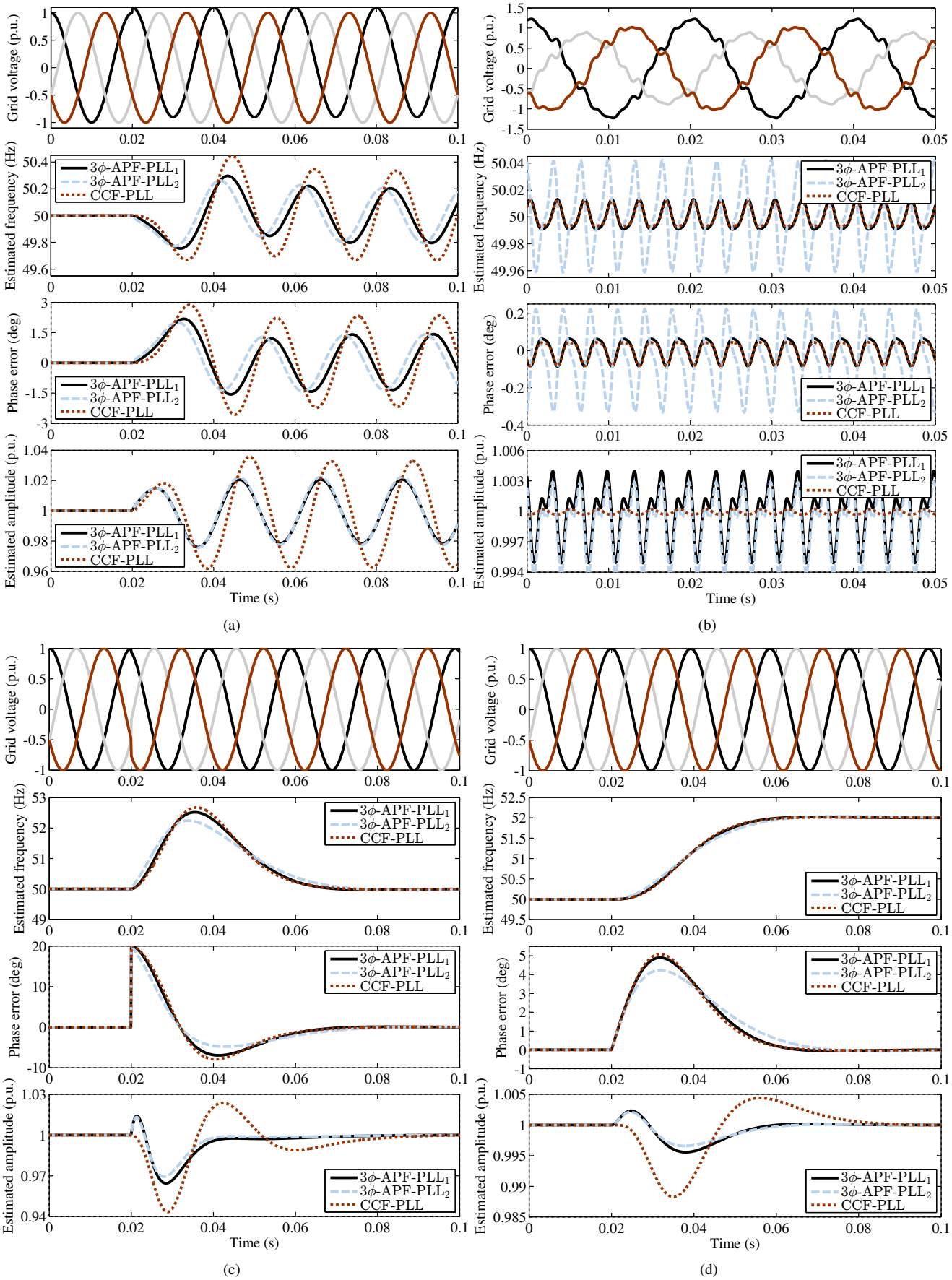

Fig. 8. A performance comparison among the 3ϕ-APF-PLL$_1$, 3ϕ-APF-PLL$_2$, and CCF-PLL. (a) Test A. (b) Test B. (c) Test C. (d) Test D.

This article has been accepted for publication in a future issue of this journal, but has not been fully edited. Content may change prior to final publication. Citation information: DOI 10.1109/TPEL.2019.2937936, IEEE Transactions on Power Electronics

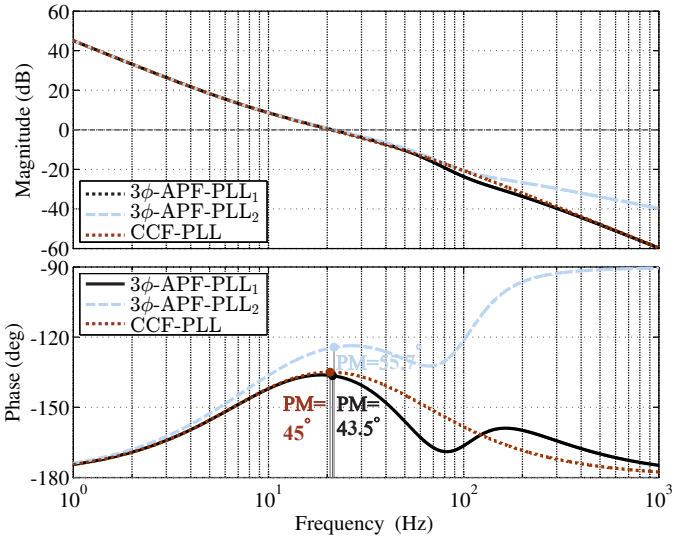

Fig. 9. Open-loop Bode plots of the 3ϕ-APF-PLL$_1$, 3ϕ-APF-PLL$_2$, and CCF-PLL. These plots are obtained using linear models shown in Fig. 5(c) and 7(b).

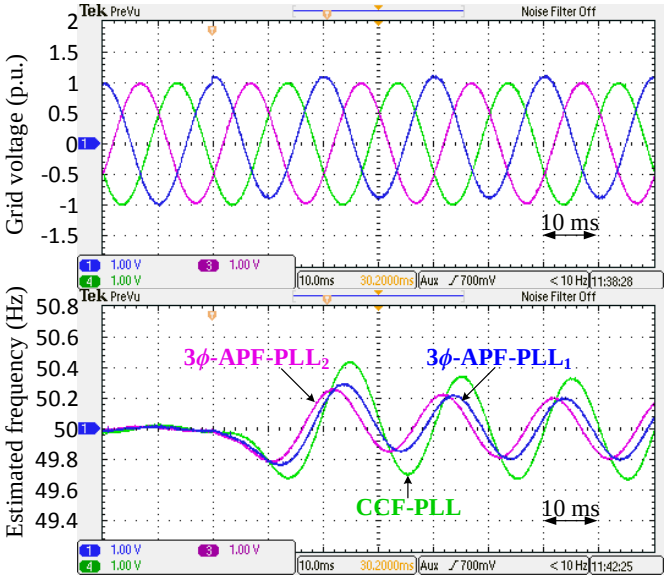

Fig. 10. Experimental performance comparison of the 3ϕ-APF-PLL$_1$, 3ϕ-APF-PLL$_2$, and CCF-PLL in response to Test A (adding 0.1 p.u. dc component to phase A).

system] is measured using a sensor board and fed to the DS2004 A/D board. The digital grid voltage signals are then normalized by dividing them by the nominal amplitude. A 0.1 p.u. dc component is then generated in the real-time code and added to the phase A. The responses of PLLs to this disturbance are sent out using DS2102 DAC board and shown on a digital oscilloscope [Tektronix DPO 2014B]. The results of this experimental test can be observed in Fig. 10. To save space, only the estimated frequencies by the PLLs are shown. As shown, these results are the same as simulation one [see Fig. 8(a)].

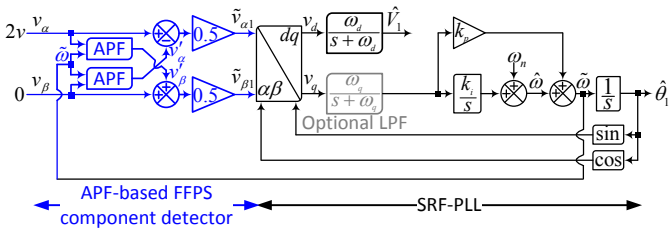

Fig. 11. Alternative mathematically-equivalent representation of the 1ϕ-APF-PLL.

III. 1ϕ-APF-PLL

A. Modeling

From Fig. 1, an alternative representation of the 1ϕ-APF-PLL can be obtained as shown in Fig. 11. This representation demonstrates that the 1ϕ-APF-PLL is actually a special case of the 3ϕ-APF-PLL where its β-axis input is equal to zero. By assuming that the single-phase grid voltage signal v is as (28), where V_1 and θ_1 are the amplitude and phase angle, respectively, the signals v_α and v_β in Fig. 11 can be expressed as (29).

$$v(t) = V_1 \cos(\theta_1) \tag{28}$$

$$\begin{aligned} v_\alpha(t) = 2v(t) &= \overbrace{\boldsymbol{V_1 \cos(\theta_1)}}^{\textbf{FFPS Com.}} + \overbrace{V_1 \cos(-\theta_1)}^{\text{FFNS Com.}} \\ v_\beta(t) = \quad 0 \quad &= \boldsymbol{V_1 \sin(\theta_1)} + V_1 \sin(-\theta_1) \end{aligned} \tag{29}$$

In (29), FFPS Com. and FFNS Com. denote the fundamental-frequency positive-sequence and negative-sequence components, respectively.

The equation (29) describes a set of imbalanced signals in the $\alpha\beta$ frame, where its positive and negative sequence components have the same amplitude. Fortunately, the FFNS component is blocked in the steady state because the transfer function between the vectors $v_\alpha(s) + jv_\beta(s)$ and $\tilde{v}_{\alpha 1}(s) + j\tilde{v}_{\beta 1}(s)$ in Fig. 11 has a zero magnitude at the fundamental negative frequency [see Fig. 4]. Therefore, the FFNS component can be neglected during the modeling procedure without significantly affecting the accuracy. Considering this fact and the similarity of Fig. 3 and 11, it can be concluded that the LTI models of 3ϕ-APF-PLL [see Fig. 5] are also valid for the 1ϕ-APF-PLL.

B. Model Verification

In this section, the accuracy of the full-order and reduced-order models of the 1ϕ-APF-PLL is investigated. As mentioned before, the 1ϕ-APF-PLL has an optional LPF in its q-axis [see Fig. 1]. The 1ϕ-APF-PLL with and without this LPF is called the 1ϕ-APF-PLL$_1$ and 1ϕ-APF-PLL$_2$, respectively. To save space, the model verification of the 1ϕ-APF-PLL$_1$ is only presented here.

Fig. 12 shows the model verification results. It is observed that both models precisely predict the dynamics of phase and frequency variables in Test 1 and 2 (i.e., the phase and frequency jump tests), and accurately anticipate the amplitude estimation dynamics in Test 3 (the voltage sag test). They, however, fail to do so in predicting the coupling between amplitude and phase/frequency variables. In the case of the

This article has been accepted for publication in a future issue of this journal, but has not been fully edited. Content may change prior to final publication. Citation information: DOI 10.1109/TPEL.2019.2937936, IEEE Transactions on Power Electronics

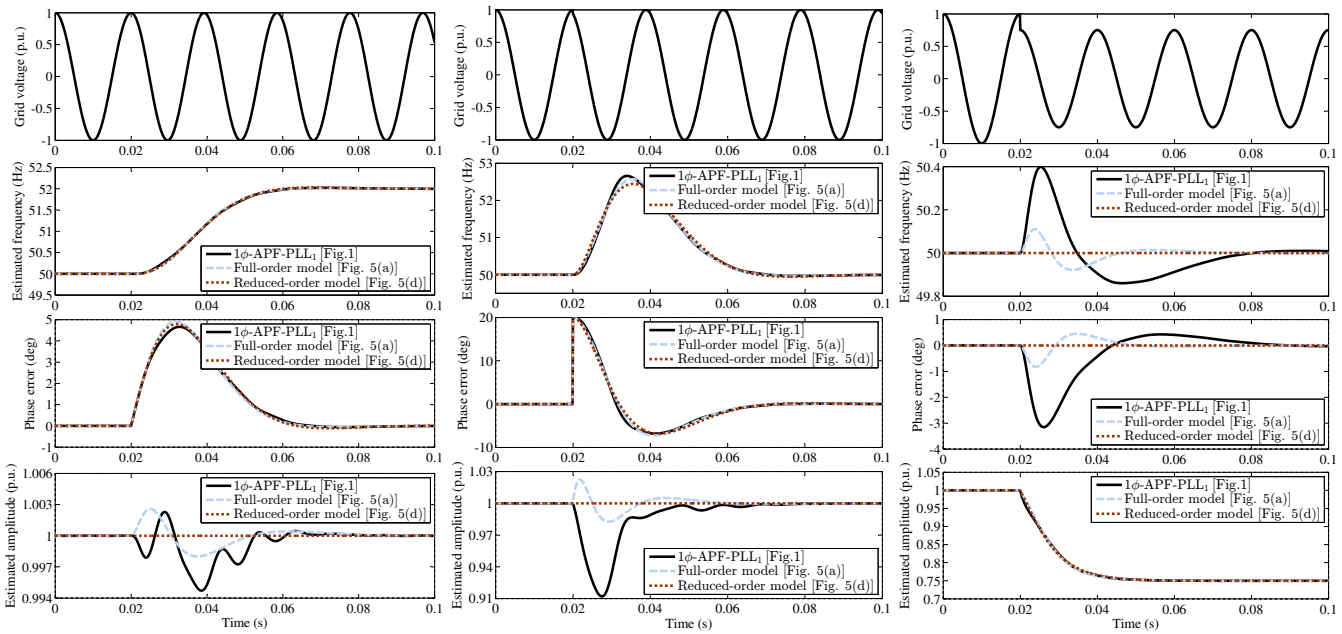

(a) (b) (c)

Fig. 12. 1ϕ-APF-PLL$_1$ model verification. (a) Test 1: 2-Hz frequency jump. (b) Test 2: 20° phase jump. (c) Test 3: 0.25 p.u. voltage sag. The control parameters of the 1ϕ-APF-PLL$_1$ can be found in Table I.

reduced-order model, this result was expected because it is obtained by neglecting the coupling terms in the full-order model. In the case of the full-order model, however, this inaccuracy requires justification, which is explained in what follows.

During the modeling of the 1ϕ-APF-PLL in Section III-A, the FFNS component highlighted in (29) was neglected. Notice that occurring a disturbance (for example, a phase, a frequency, or an amplitude jump) results in a change in this FFNS component, which affects the 1ϕ-APF-PLL transient response. The full-order model, however, does not consider this component and, therefore, cannot predict its effects. It is worth mentioning here that considering the FFNS component during the modeling procedure results in a linear-time periodic (LTP) model, which is more complicated to analyze compared to LTI models developed in this paper. For more details about the LTP modeling of single-phase grid synchronization systems, refer to [23].

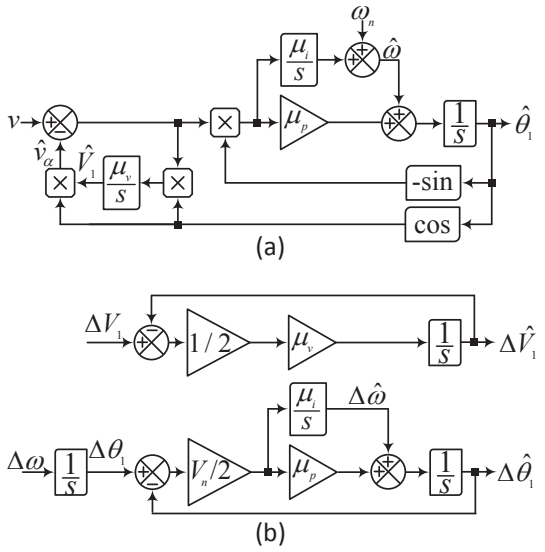

Fig. 13. (a) Block diagram representation of the EPLL. (b) EPLL LTI model. μ_p, μ_i, and μ_v are the EPLL control parameters.

C. Performance Comparison

In this section, a comparison among the 1ϕ-APF-PLL$_1$, 1ϕ-APF-PLL$_2$ and enhanced PLL (EPLL) [5], [24], which is a well-known single-phase PLL, is conducted. The block diagram of the EPLL and its linear model may be observed in Fig. 13.

Equation (30) is the EPLL closed-loop transfer function, which can be obtained from its LTI model.

$$G_{cl}^{\text{EPLL}}(s) = \frac{\Delta\hat{\theta}_1(s)}{\Delta\theta_1(s)} = \frac{0.5V_n(\mu_p s + \mu_i)}{s^2 + 0.5V_n\mu_p s + 0.5V_n\mu_i} \quad (30)$$

If we compare the above transfer function with (25) or (26),[6] it can be concluded that a fair comparison between the EPLL and 1ϕ-APF-PLL$_1$/1ϕ-APF-PLL$_2$ demands $\mu_p = 2k_p$ and $\mu_i = 2k_i$. Table I summarizes the control parameters of all these PLLs.

Four numerical tests are conducted.

[6]The equations (25) or (26) are the (approximate) closed-loop transfer functions of the 3ϕ-APF-PLL$_2$ and 3ϕ-APF-PLL$_1$, respectively, which are obtained from their reduced-order LTI model [see Fig. 5(d)]. As the 1ϕ-APF-PLL and 3ϕ-APF-PLL have the same models, it can be concluded that these transfer functions are valid for the 1ϕ-APF-PLL$_2$ and 1ϕ-APF-PLL$_1$ too.

This article has been accepted for publication in a future issue of this journal, but has not been fully edited. Content may change prior to final publication. Citation information: DOI 10.1109/TPEL.2019.2937936, IEEE Transactions on Power Electronics

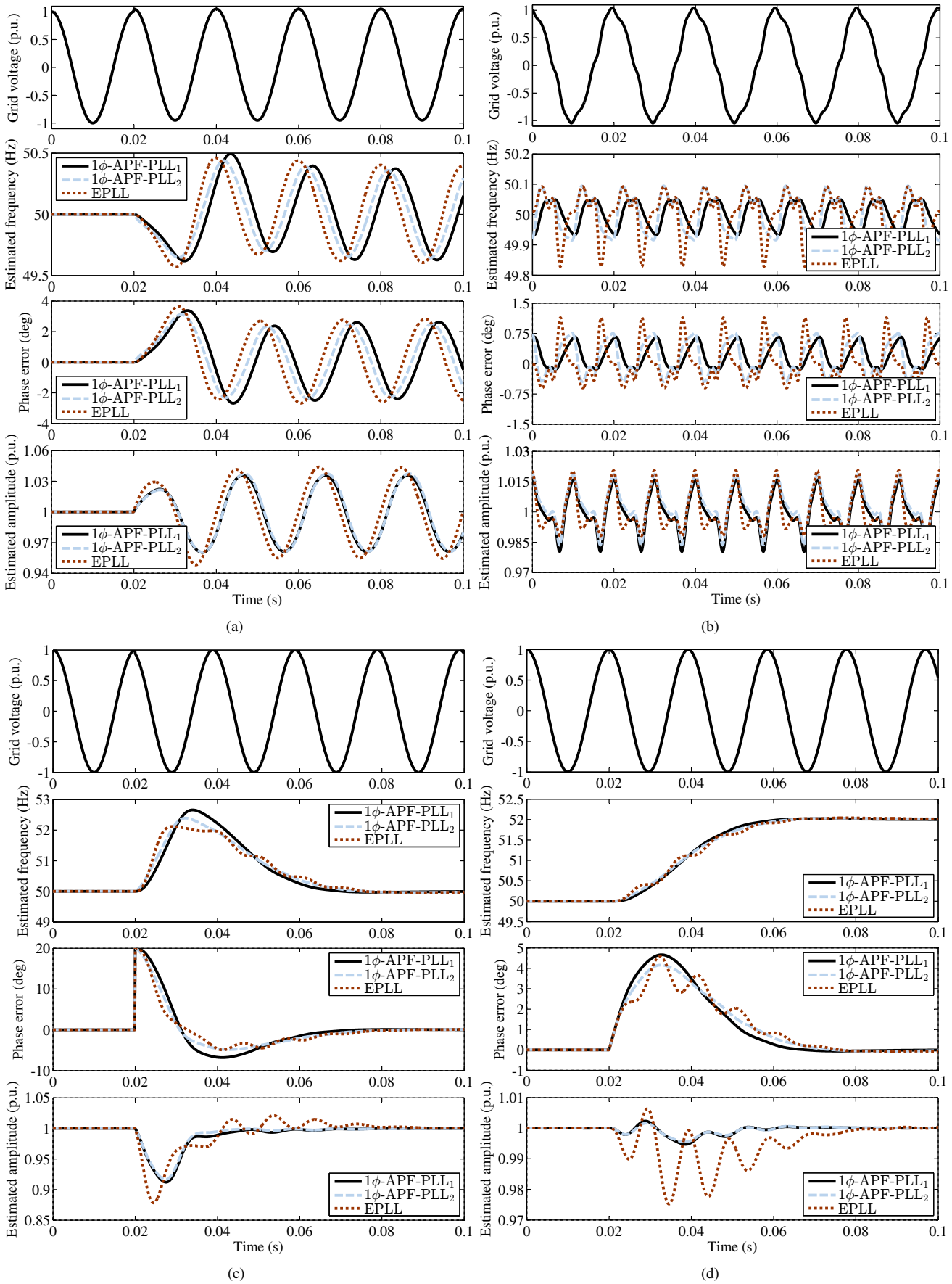

Fig. 14. A performance comparison among the 1ϕ-APF-PLL$_1$, 1ϕ-APF-PLL$_2$, and EPLL. (a) Test A*. (b) Test B*. (c) Test C*. (d) Test D*.

This article has been accepted for publication in a future issue of this journal, but has not been fully edited. Content may change prior to final publication. Citation information: DOI 10.1109/TPEL.2019.2937936, IEEE Transactions on Power Electronics

TABLE III
STABILITY MARGINS OF 1ϕ-APF-PLL$_1$, 1ϕ-APF-PLL$_2$, AND EPLL AND DETAILS OF THEIR NUMERICAL COMPARISON

	1ϕ-APF-PLL$_1$	1ϕ-APF-PLL$_2$	EPLL
Test A*: DC offset			
Peak-to-peak frequency error	0.75 Hz	0.71 Hz	0.79 Hz
Peak-to-peak phase error	5.02°	4.79°	5.37°
Peak-to-peak amplitude error	0.07 p.u.	0.08 p.u.	0.09 p.u.
Test B*: Harmonics			
Peak-to-peak frequency error	0.12 Hz	0.18 Hz	0.26 Hz
Peak-to-peak phase error	0.8°	1.2°	1.74°
Peak-to-peak amplitude error	0.04 p.u.	0.04 p.u.	0.03 p.u.
Test C*: Phase jump			
2% settling time	48.1 ms	54.6 ms	56 ms
Phase overshoot	34.06%	24.31%	24.65%
Peak frequency variation	2.66 Hz	2.39 Hz	2.12 Hz
Peak amplitude variation	0.09 p.u.	0.08 p.u.	0.12 p.u.
Test D*: Frequency jump			
2% settling time	38.4 ms	40.7 ms	43.1 ms
Frequency overshoot	1.06%	1.64%	2.07%
Peak phase variation	4.66°	4.16°	4.57°
Peak amplitude variation	0.01 p.u.	0.01 p.u.	0.02 p.u.
Phase margin	43.5°	55.7°	68.9°

Note: All results are rounded to 2 decimal places.

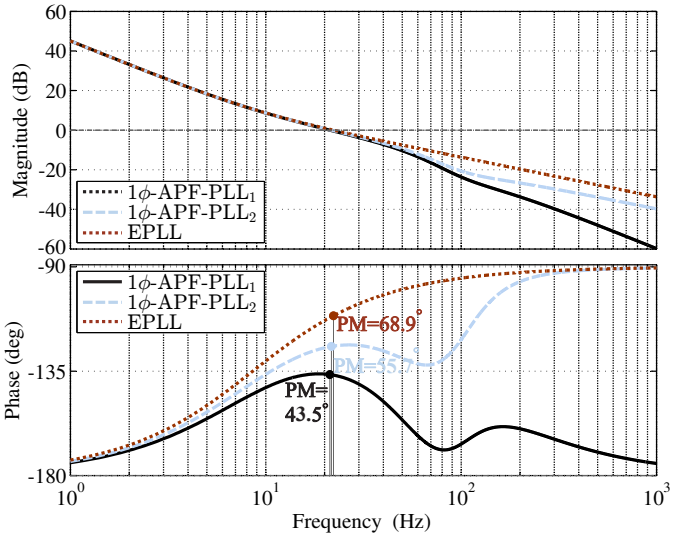

Fig. 15. Open-loop Bode plots of the 1ϕ-APF-PLL$_1$, 1ϕ-APF-PLL$_2$, and EPLL. These plots are obtained using the linear models shown in Fig. 5(c) and 13(b).

- In **Test A***, a 0.05 p.u. dc component is suddenly added to the PLLs input signal.
- In **Test B***, the input signal is contaminated with low-order harmonics of order 3, 5, 7, and 9. The amplitudes of these harmonics are 5%, 4%, 3%, and 2%, respectively, which are corresponding to a total harmonic distortion around 7.35%.
- In **Test C***, a 20° phase jump in the PLLs input signal happens.
- In **Test D***, a 2-Hz frequency jump in the PLLs input signal occurs.

The results of these tests and their details can be found in Fig. 14 and Table III, respectively. From these results, the following observations are made.

- All PLLs demonstrate a close level of dc-offset filtering capability.
- The 1ϕ-APF-PLL$_1$, thanks to its in-loop LPF, represents a slightly better performance than the 1ϕ-APF-PLL$_2$ and EPLL in filtering harmonics.
- The 1ϕ-APF-PLL$_1$ demonstrates a larger phase overshoot than the 1ϕ-APF-PLL$_2$ and EPLL after the phase jump. The main reason behind this observation is the phase delay caused by its in-loop LPF, which reduces its phase margin. This fact is clear from Fig. 15.
- There is not a large difference between the settling time of 1ϕ-APF-PLL$_1$, 1ϕ-APF-PLL$_2$, and EPLL during transients.

IV. MFOF-PLL

A. Description and Modeling

The MFOF, which is used for generating the fictitious quadrature signal in the MFOF-PLL [see Fig. 2], is expressed in the Laplace domain as [15]

$$G_{\text{MFOF}}(s) = \frac{\omega - ks}{s + k\omega} \tag{31}$$

where k is the design constant of this filter, and ω is the grid voltage angular frequency. Notice that, as shown in Fig. 2, the estimated frequency is fed back to the MFOF to adapt it to frequency variations.

Fig. 16 shows the MFOF frequency response for three different values of k. From this plot and the transfer function (31), the following observations are made:

- Regardless of the value of k, the MFOF has $-90°$ phase at the fundamental frequency.
- $k = 1$ results in a unity amplitude at all frequencies and therefore make the MFOF a first-order APF.
- $0 \leq k < 1$ amplifies the dc component and sub-harmonics and attenuates frequencies larger than the fundamental frequency. Notice that $k = 0$ makes the MFOF an ideal integrator.
- $k > 1$ attenuates the dc component and sub-harmonics and amplifies frequencies larger than the fundamental frequency. Notice that $k = \infty$ makes the MFOF a differentiator.

Fig. 17 illustrates an alternative mathematically-equivalent representation of the MFOF-PLL. Considering this structure, the discussions conducted in Section III-A, and the mathematical modeling procedure presented in Section II-A, the full-order model of the MFOF-PLL can be obtained as shown in Fig. 18(a). By applying the block diagram algebra, this model can be rearranged as Fig. 18(b). Neglecting the cross-coupling terms leads to Fig. 18(c). Further simplification can be achieved by replacing the second-order transfer functions in Fig. 18(c) by their first-order approximations, as depicted in Fig. 18(d). These models are useful for measuring the stability margin of the MFOF-PLL, tuning its control parameters, and analyzing its performance. The accuracy of these models can be verified using numerical results. To save space, the model verification results are not presented here.

This article has been accepted for publication in a future issue of this journal, but has not been fully edited. Content may change prior to final publication. Citation information: DOI 10.1109/TPEL.2019.2937936, IEEE Transactions on Power Electronics

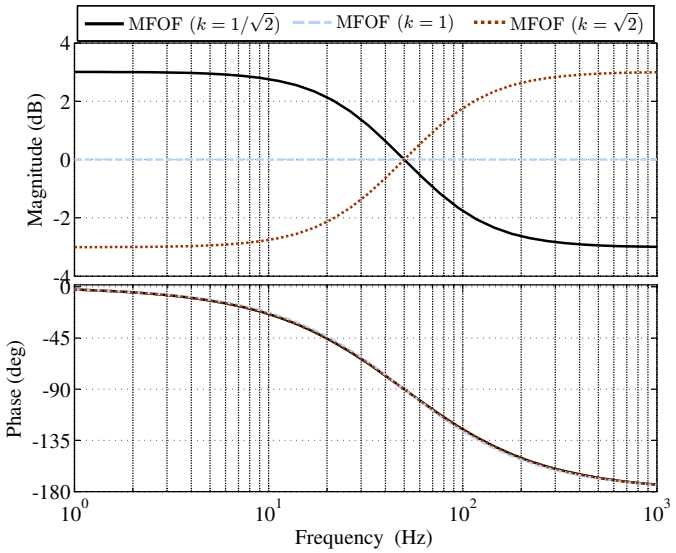

Fig. 16. Frequency response of the MFOF for three different values of k.

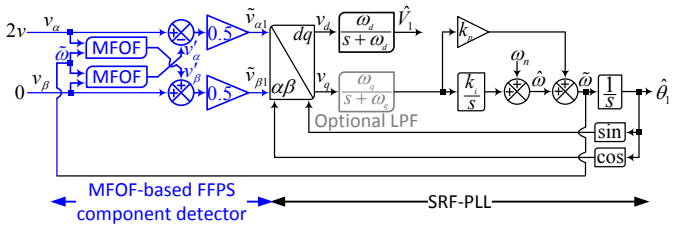

Fig. 17. Alternative mathematically-equivalent representation of the MFOF-PLL.

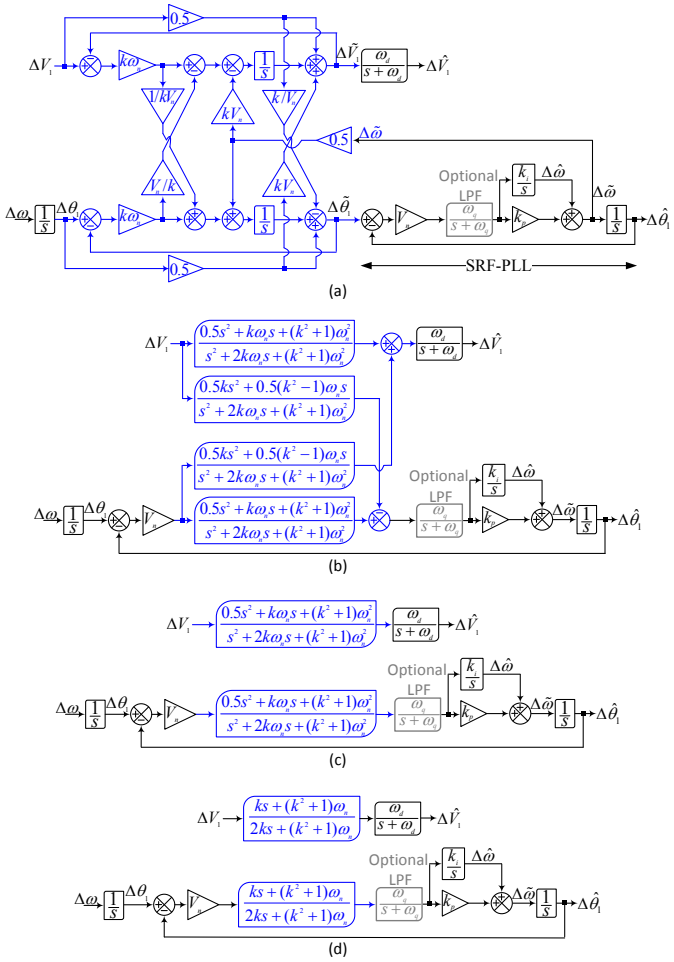

Fig. 18. (a) Full-order linear model of the MFOF-PLL. (b) Alternative representation of the full-order model. (c) Neglecting the coupling terms of the model. (d) Reduced-order linear model of the MFOF-PLL.

B. Performance Assessment

As discussed before, the only difference of the MFOF-PLL compared to the 1ϕ-APF-PLL is the additional degree of freedom k in its structure [see Figs. 1 and 2]. This section aims to investigate the effects of this additional degree of freedom. To this end, the following cases are considered:

- MFOF-PLL$_1$: $k=1/\sqrt{2}$
- MFOF-PLL$_2$: $k=1$
- MFOF-PLL$_3$: $k=\sqrt{2}$.

In all these cases, the optional LPF in the q-axis is neglected. Notice that, as mentioned before, $k=1$ makes the MFOF a first-order APF. Therefore, the MFOF-PLL$_2$ and the 1ϕ-APF-PLL$_2$ are the same systems. Considering this fact, the control parameters of the MFOF-PLL$_2$ are selected the same as those of the 1ϕ-APF-PLL$_2$ [see Table I]. As the objective here is to investigate the effects of the parameter k, the proportional and integral gains of the MFOF-PLL$_1$ and MFOF-PLL$_3$ and the cutoff frequency of their d-axis LPF are chosen the same as those of the MFOF-PLL$_2$.

The same tests as those defined in Section III-C are considered for the investigation here. Fig. 19 shows the results of these tests, and Table IV summarizes the details of the results. From these results, the following observations are made:

- MFOF-PLL$_1$ and MFOF-PLL$_3$, which have the lowest and highest value of k, have the worst and best dc-offset filtering capability, respectively. This result is consistent with the MFOF bode plot [see Fig. 16].
- From the harmonic filtering capability point of view, the MFOF-PLL$_1$ has the best performance, and the MFOF-PLL$_3$ has the worst one. Again, this result is consistent with the MFOF frequency response [see Fig. 16].
- There is not a large difference between the dynamic response and stability margin of the MFOF-PLL$_1$, MFOF-PLL$_2$, and MFOF-PLL$_3$.

V. Conclusion

In this paper, a study on APF-based PLL systems was conducted. The focus of the study was first on the 3ϕ-APF-PLL. Through a detailed mathematical procedure, an accurate model (called the full-order model) for the 3ϕ-APF-PLL was developed for the first time. The remarkable accuracy of this model was proved through some numerical tests in Matlab/Simulink environment. To simplify the analysis and the tuning procedure, a reduced-order model for the 3ϕ-APF-PLL was proposed. Some control design guidelines were then presented. Finally, to highlight the advantages and disadvantages of the 3ϕ-APF-PLL, some comparative numerical and

This article has been accepted for publication in a future issue of this journal, but has not been fully edited. Content may change prior to final publication. Citation information: DOI 10.1109/TPEL.2019.2937936, IEEE Transactions on Power Electronics

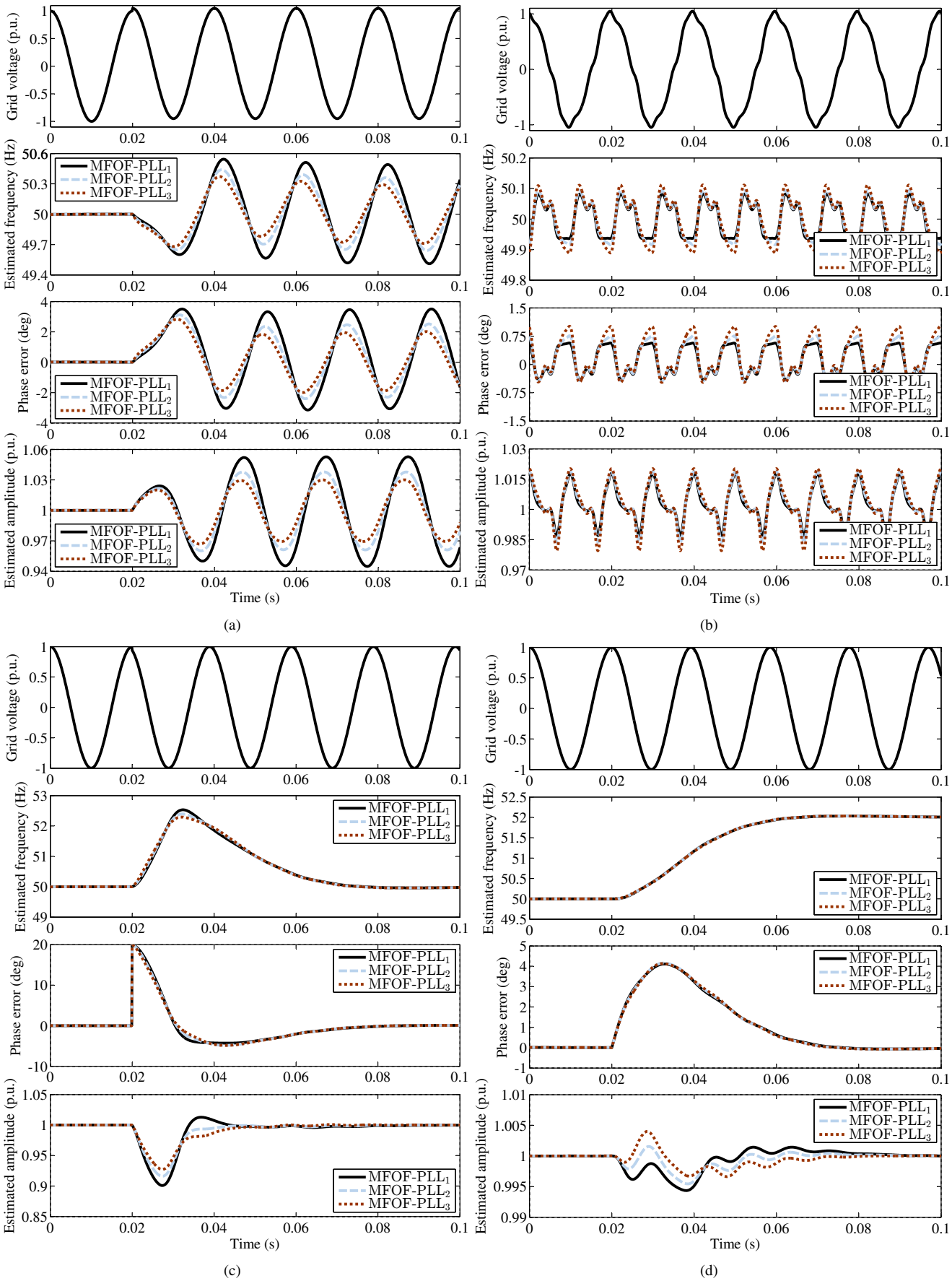

Fig. 19. MFOF-PLL performance investigation for different values of the parameter k. (a) Test A*. (b) Test B*. (c) Test C*. (d) Test D*.

This article has been accepted for publication in a future issue of this journal, but has not been fully edited. Content may change prior to final publication. Citation information: DOI 10.1109/TPEL.2019.2937936, IEEE Transactions on Power Electronics

TABLE IV
STABILITY MARGINS OF MFOF-PLL$_1$, MFOF-PLL$_2$, AND MFOF-PLL$_3$ AND DETAILS OF THEIR NUMERICAL COMPARISON

	MFOF-PLL$_1$	**MFOF-PLL$_2$**	**MFOF-PLL$_3$**
Test A*: DC offset			
Peak-to-peak frequency error	0.98 Hz	0.71 Hz	0.58 Hz
Peak-to-peak phase error	6.56°	4.79°	3.88°
Peak-to-peak amplitude error	0.11 p.u.	0.08 p.u.	0.06 p.u.
Test B*: Harmonics			
Peak-to-peak frequency error	0.15 Hz	0.18 Hz	0.22 Hz
Peak-to-peak phase error	0.98°	1.2°	1.48°
Peak-to-peak amplitude error	0.03 p.u.	0.04 p.u.	0.04 p.u.
Test C*: Phase jump			
2% settling time	55.6 ms	54.6 ms	54.7 ms
Phase overshoot	21.57%	24.31%	24.35%
Peak frequency variation	2.53 Hz	2.39 Hz	2.29 Hz
Peak amplitude variation	0.1 p.u.	0.08 p.u.	0.07 p.u.
Test D*: Frequency jump			
2% settling time	41.1 ms	40.7 ms	40.6 ms
Frequency overshoot	1.62%	1.64%	1.71%
Peak phase variation	4.11°	4.16°	4.13°
Peak amplitude variation	0.01 p.u.	0.01 p.u.	0 p.u.
Phase margin	57°	55.7°	58.6°

Note: All results are rounded to 2 decimal places.

experimental tests were conducted. As a reference for the comparison, a typical CCF-PLL, which is a well-known three-phase PLL, was considered.

In the second part of this research, the focus was on the 1ϕ-APF-PLL. It was demonstrated that the 1ϕ-APF-PLL is a special case of the 3ϕ-APF-PLL where its β-axis input is equal to zero. Based on this fact, it was concluded that the models developed for the 3ϕ-APF-PLL are also valid for the 1ϕ-APF-PLL. This conclusion was verified using numerical tests. Finally, to gain insight into the advantages/disadvantages of the 1ϕ-APF-PLL, a performance comparison with the EPLL, which is a popular single-phase PLL, was carried out.

In the last part of this study, the focus was on the MFOF-PLL, which is implemented by adding a degree of freedom (parameter k) to the 1ϕ-APF-PLL. It was discussed that the modeling of the MFOF-PLL can be carried out by following the same procedure as that explained for the case of the 3ϕ-APF-PLL. It was also demonstrated using numerical tests that the additional degree of freedom of the MFOF-PLL is a means for adjusting its dc/harmonic filtering capability without significantly affecting its dynamic response and stability margin compared to the 1ϕ-APF-PLL. A hidden assumption here is that the parameter k is close to unity.

In summary, this paper disseminates useful knowledge about modeling and tuning of APF-based PLLs and highlights their pros and cons compared to the state-of-the-art PLL systems. Therefore, it can be a good reference for researchers who work in this area.

ACKNOWLEDGMENT

This project was funded by the Deanship of Scientific Research (DSR) at King Abdulaziz University, Jeddah, under grant no. (RG-9-135-38). The authors, therefore, acknowledge with thanks DSR technical and financial support.

REFERENCES

[1] W. Xiao, M. S. El Moursi, O. Khan, and D. Infield, "Review of grid-tied converter topologies used in photovoltaic systems," *IET Renew. Power Gener.*, vol. 10, no. 10, pp. 1543–1551, 2016.

[2] F. Blaabjerg, R. Teodorescu, M. Liserre, and A. V. Timbus, "Overview of control and grid synchronization for distributed power generation systems," *IEEE Trans. Ind. Electron.*, vol. 53, no. 5, pp. 1398–1409, Oct. 2006.

[3] S. Golestan, J. M. Guerrero, and J. C. Vasquez, "Single-phase PLLs: A review of recent advances," *IEEE Trans. Power Electron.*, vol. 32, no. 12, pp. 9013–9030, Dec. 2017.

[4] S. Golestan, J. M. Guerrero, and J. C. Vasquez, "Three-phase PLLs: A review of recent advances," *IEEE Trans. Power Electron.*, vol. 32, no. 3, pp. 1894–1907, Mar. 2017.

[5] M. Karimi-Ghartemani, *Enhanced phase-locked loop structures for power and energy applications*. John Wiley & Sons, 2014.

[6] S. Golestan, J. M. Guerrero, A. Abusorrah, M. M. Al-Hindawi, and Y. Al-Turki, "An adaptive quadrature signal generation-based single-phase phase-locked loop for grid-connected applications," *IEEE Trans. Ind. Electron.*, vol. 64, no. 4, pp. 2848–2854, Apr. 2017.

[7] S. Golestan, J. M. Guerrero, J. C. Vasquez, A. M. Abusorrah, and Y. Al-Turki, "Research on variable-length transfer delay and delayed-signal-cancellation-based PLLs," *IEEE Trans. Power Electron.*, vol. 33, no. 10, pp. 8388–8398, Oct. 2018.

[8] M. Ciobotaru, R. Teodorescu, and F. Blaabjerg, "A new single-phase PLL structure based on second order generalized integrator," in *2006 37th IEEE Power Electronics Specialists Conference*, Jun. 2006, pp. 1–6.

[9] Q. Guan, Y. Zhang, Y. Kang, and J. M. Guerrero, "Single-phase phase-locked loop based on derivative elements," *IEEE Trans. Power Electron.*, vol. 32, no. 6, pp. 4411–4420, Jun. 2017.

[10] S. Golestan, M. Monfared, F. D. Freijedo, and J. M. Guerrero, "Dynamics assessment of advanced single-phase PLL structures," *IEEE Trans. Ind. Electron.*, vol. 60, no. 6, pp. 2167–2177, Jun. 2013.

[11] R. M. S. Filho, P. F. Seixas, P. C. Cortizo, L. A. B. Torres, and A. F. Souza, "Comparison of three single-phase PLL algorithms for UPS applications," *IEEE Trans. Ind. Electron.*, vol. 55, no. 8, pp. 2923–2932, Aug. 2008.

[12] Y. Jung, J. So, G. Yu, and J. Choi, "Modelling and analysis of active islanding detection methods for photovoltaic power conditioning systems," in *Canadian Conference on Electrical and Computer Engineering 2004*, vol. 2, May. 2004, pp. 979–982.

[13] J.-W. Choi, Y.-K. Kim, and H.-G. Kim, "Digital PLL control for single-phase photovoltaic system," *IEE Proc.-Electric Power Appl.*, vol. 153, no. 1, pp. 40–46, Jan. 2006.

[14] S. Kim and S. Sul, "Control of rubber tyred gantry crane with energy storage based on supercapacitor bank," *IEEE Trans. Power Electron.*, vol. 21, no. 5, pp. 1420–1427, Sep. 2006.

[15] D. Stojic, N. Georgijevic, M. Rivera, and S. Milic, "Novel orthogonal signal generator for single phase PLL applications," *IET Power Electronics*, vol. 11, no. 3, pp. 427–433, 2018.

[16] S.-J. Lee, J.-K. Kang, and S.-K. Sul, "A new phase detecting method for power conversion systems considering distorted conditions in power system," in *Proc. Industry Applications Conf., 34th IAS Annu. Meeting*, vol. 4, Oct. 1999, pp. 2167–2172.

[17] H. Sagha, G. Ledwich, A. Ghosh, and G. Nourbakhsh, "A frequency adaptive single-phase phase-locked loop with harmonic rejection," in *IEEE IECON 2014*, Oct. 2014, pp. 1028–1033.

[18] P. Rodriguez, R. Teodorescu, I. Candela, A. V. Timbus, M. Liserre, and F. Blaabjerg, "New positive-sequence voltage detector for grid synchronization of power converters under faulty grid conditions," in *2006 37th IEEE Power Electronics Specialists Conference*, Jun. 2006, pp. 1–7.

[19] S. Golestan, M. Monfared, and F. D. Freijedo, "Design-oriented study of advanced synchronous reference frame phase-locked loops," *IEEE Trans. Power Electron.*, vol. 28, no. 2, pp. 765–778, Feb. 2013.

[20] V. Kaura and V. Blasko, "Operation of a phase locked loop system under distorted utility conditions," *IEEE Trans. Ind. Appl.*, vol. 33, no. 1, pp. 58–63, Jan. 1997.

[21] X. Guo, W. Wu, and Z. Chen, "Multiple-complex coefficient-filter-based phase-locked loop and synchronization technique for three-phase grid-interfaced converters in distributed utility networks," *IEEE Trans. Ind. Electron.*, vol. 58, no. 4, pp. 1194–1204, Apr. 2011.

[22] M. Ramezani, S. Golestan, S. Li, and J. M. Guerrero, "A simple approach to enhance the performance of complex-coefficient filter-based PLL in grid-connected applications," *IEEE Trans. Ind. Electron.*, vol. 65, no. 6, pp. 5081–5085, Jun. 2018.

[23] S. Golestan, J. M. Guerrero, and J. C. Vasquez, "Modeling and stability assessment of single-phase grid synchronization techniques: Linear time-periodic versus linear time-invariant frameworks," *IEEE Trans. Power Electron.*, vol. 34, no. 1, pp. 20–27, Jan. 2019.

[24] M. Karimi-Ghartemani, "Linear and pseudolinear enhanced phased-locked loop (EPLL) structures," *IEEE Trans. Ind. Electron.*, vol. 61, no. 3, pp. 1464–1474, Mar. 2014.